

Phonons in Bi₂S₃ nanostructures: Raman scattering and first-principles studiesYanyuan Zhao,¹ Kun Ting Eddie Chua,² Chee Kwan Gan,² Jun Zhang,¹ Bo Peng,¹
Zeping Peng,³ and Qihua Xiong^{1,4,*}¹*Division of Physics and Applied Physics, School of Physical and Mathematical Sciences, Nanyang Technological University,
21 Nanyang Link, Singapore 637371*²*Institute of High Performance Computing, 1 Fusionopolis Way, #16-16 Connexis, Singapore 138632*³*School of Physical Science and Technology, MOE Key Laboratory on Luminescence and Real-Time Analysis,
Southwest University, Chongqing 400715, China*⁴*Division of Microelectronics, School of Electrical and Electronic Engineering, Nanyang Technological University,
Singapore 639798*

(Received 1 July 2011; revised manuscript received 30 October 2011; published 21 November 2011)

Bi₂S₃ has shown promise in thermoelectric and optoelectronic applications as well as biological and chemical sensors. We present here a comprehensive study on the lattice dynamics of Bi₂S₃ nanostructures probed by micro-Raman scattering spectroscopy and first-principles calculations. Bi₂S₃ nanowires are synthesized using a physical vapor transport method via a vapor-liquid-solid mechanism on silicon substrates. Oriented Bi₂S₃ nanosheets are also obtained on mica substrates. The structure of the nanowires is determined to be orthorhombic with a growth orientation of [110] by x-ray diffraction and high-resolution transmission electron microscopy. A Raman scattering study is conducted for as-prepared Bi₂S₃ nanostructures, in which 33, 38, 46, and 53 cm⁻¹ phonon modes are observed for the first time. We find several modes to be very sensitive to excitation wavelength and power. First-principles calculations of orthorhombic Bi₂S₃ predict a series of Raman modes, in good agreement with our experiments. Phonon-dispersion curves of Bi₂S₃ are also presented, and the effect of Born effective charges on the longitudinal-optical–transverse-optical splitting at the zone center is taken into account.

DOI: [10.1103/PhysRevB.84.205330](https://doi.org/10.1103/PhysRevB.84.205330)

PACS number(s): 78.30.Fs, 63.20.D–, 71.15.Mb, 62.23.Kn

I. INTRODUCTION

In the past decades, semiconductor nanomaterials have been the focus of nanoscience and nanotechnology due to their unique chemical and physical properties and potential applications in a variety of fields. The metal chalcogenides A₂B₃^{VI} (A = As, Sb, Bi; B = S, Se, Te) form an important class of semiconductors that have extensive applications in photovoltaics,^{1,2} optoelectronics,³ and thermoelectricity.⁴ The investigation of metal chalcogenide compounds is a very active research area with relevance to both fundamental and application-related issues.⁵ With a direct band gap of 1.3 eV, bismuth sulfide (Bi₂S₃) exhibits promising applications in photovoltaic converters and thermoelectric cooling technologies based on the Peltier effect.⁴ Recently, Bi₂S₃ nanostructures have been used in x-ray computed tomography imaging,⁶ gas sensing,⁷ and biomolecule detection.⁸ Thus far, studies on Bi₂S₃ have focused mainly on the synthesis and applications of its physical and chemical properties. Other fundamental properties, such as the rarely reported lattice dynamics, are equally indispensable in order to understand and engineer its optical and electrical properties via electron-phonon and photon-phonon interactions. Raman scattering spectroscopy is nondestructive and highly sensitive to structural defects⁹ and structural anisotropy in nanostructures (e.g., surface phonons activated by surface modulation,^{10–12} phonon splitting, and the antenna effect,¹³ etc.). Raman spectroscopy is also very powerful for studying phonons in atomic layered materials, such as graphene¹⁴ and, most recently, topological insulators.¹⁵ In this regard, Raman scattering spectroscopy is versatile and ideal for studying phonons in Bi₂S₃. To the best of our knowledge, there

has been no systematic Raman study of Bi₂S₃. Although there exist scattered reports about Raman scattering for Bi₂S₃ in both powder form and nanostructure form,^{6,16–20} the identification of these phonon modes is lacking. From a fundamental level, the full picture of the phonon dispersion and dynamics is missing.

A variety of Bi₂S₃ nanostructures have been synthesized, including nanoparticles,⁶ nanowires,^{7,8,21–23} nanorods,^{19,24} nanotubes,²⁵ nanoribbons,²⁶ nanoflowers,¹⁷ etc., in which different methods including hydrothermal,²⁷ metal organic chemical vapor deposition,²⁸ the solution-gas interface technique,¹ and the electrodeposition method are involved.²⁹ Bi₂S₃ nanoarrays have been made by employing the electrodeposition techniques with an anodic alumina membrane (AMM).^{2,30} The above-mentioned methods are largely chemistry-based. However, there have been few reports on the physical vapor transport method, which results in less incorporation of organic and ligand impurities in comparison with the wet chemical methods.

In this work, a physical vapor transport method has been employed to synthesize Bi₂S₃ nanostructures. High-crystallinity nanowires and oriented nanosheets have been obtained on both Si and mica substrates. A comprehensive study on the lattice vibrational properties of Bi₂S₃ is conducted based on those high-quality nanomaterials. We present here an experimental micro-Raman scattering study together with theoretical calculations of Bi₂S₃ single crystals with the aim to study the lattice dynamics for photoelectronic and thermoelectric investigations. First-principles calculations for vibrational modes of orthorhombic Bi₂S₃ predict

a series of Raman-active phonon modes that are in good agreement with our experiment. Phonon-dispersion curves of Bi_2S_3 are also calculated via density-functional theory (DFT).

II. MATERIALS AND METHODS

A. Sample preparation and characterizations

Bi_2S_3 nanostructures were synthesized via physical vapor transport in a hot-walled horizontal tube furnace. Bulk Bi_2S_3 powder (Aldrich 99.9%) was placed at the center of the furnace in a quartz boat. The synthesis was carried out at 455 °C with a H_2 carrier gas flow of 20 sccm at 5 torr for 30 min. The product was collected at the downstream end of the furnace on substrates. Both Si (100) and mica substrates were used for the growth of the Bi_2S_3 nanostructures. Si substrates were first treated with poly-L-lysine to form positively charged surfaces before the gold nanoparticle (50 nm, Ted Pella) dispersion. Freshly cleaved mica substrates were applied without any treatments.

The morphology of the products was examined by scanning electron microscopy (SEM, JEOL 7001F). Figure 1(a) shows an SEM image of as-prepared Bi_2S_3 nanowires on Si substrates. The gold nanoparticle on top of the nanowire shown as the inset demonstrates the vapor-liquid-solid (VLS) growth mode. The diameter of as-grown nanowires is 40–60 nm, consistent with the diameter of the Au nanoparticles, and the length is 4–7 μm . In addition to the VLS growth mechanism, there also exists catalyst-free vapor deposition, in which case the diameter sizes of the Bi_2S_3 wires show a fairly large variation from tens of nanometers to hundreds of nanometers, as shown in the low magnification picture. Mica is a layered structure material with natural atomic flatness, and it has been demonstrated to introduce the epitaxial growth of cadmium chalcogenide nanowire arrays.³¹ Using mica as substrates, nanowires and oriented nanosheets can be obtained, as shown in Fig. 1(b). The nanosheets grow along the surface of mica. The orientations and sharp facets of the micrometer-scale surfaces are shown in the top-right inset. Bi_2S_3 nanowires

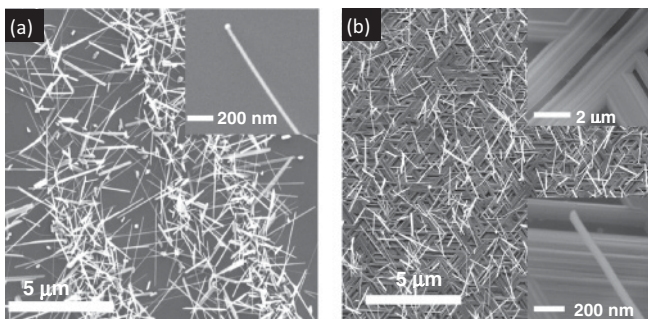


FIG. 1. (a) Bi_2S_3 nanowires grown on Si substrates. The nanowires have a uniform diameter of ~ 50 nm and a length of 4–7 μm . The inset shows a gold nanoparticle on top of the nanowire, demonstrating the VLS growth mechanism. (b) Bi_2S_3 nanowires and nanosheets grown on mica substrates. The nanosheets are lying on mica with orientations. The diameter of the nanowires is 50–100 nm and the length is 3–5 μm . The insets show a nanowire under high magnification and directionally grown nanosheets.

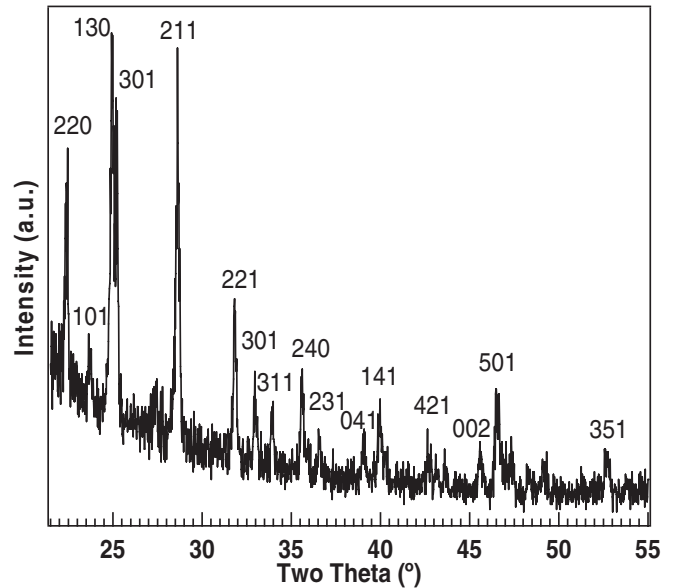


FIG. 2. XRD spectrum of as-prepared Bi_2S_3 nanostructures. The peaks are identified to be an orthorhombic structure (JCPDS 17-0320).

grown on top of the nanosheet layer through catalyst-free vapor deposition exhibit diameter sizes mainly between 50 and 100 nm.

The structure of as-prepared Bi_2S_3 nanostructures was examined using x-ray diffraction (XRD) (Bruker D8 advanced diffractometer, $\text{Cu } K\alpha$) and transmission electron microscopy (TEM, JEOL 2010F). The XRD spectrum shown in Fig. 2 indicates that the products on both Si and mica substrates are in the orthorhombic phase (JCPDS card No. 17-0320) with good crystallinity. To obtain additional information about the growth orientation, we conducted a detailed TEM analysis. Figure 3(b) displays TEM images of an individual 50 nm Bi_2S_3 nanowire. Figure 3(a) is a magnified view showing clearly the lattice fringes. Figure 3(c) is a selected area electron diffraction (SAED) pattern of this nanowire. High-resolution transmission electron microscopy (HRTEM) analysis suggests that nanowires grow along the [110] orientation.

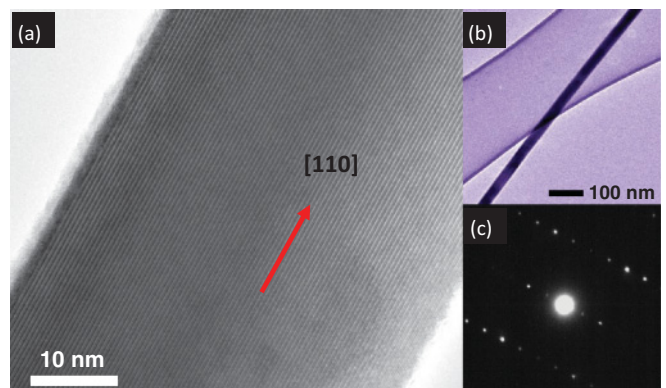


FIG. 3. (Color online) HRTEM (a) and TEM (b) images of an as-grown Bi_2S_3 nanowire with a diameter of 50 nm, which grows along the [110] direction. (c) SAED pattern taken from the same nanowire.

B. Raman measurement

Raman scattering spectroscopy was conducted at room temperature using a micro-Raman spectrometer (Horiba-JY T64000) in a backscattering configuration. Three different lasers have been used to excite the sample: a He-Ne laser ($\lambda = 632.8$ nm), a solid-state laser ($\lambda = 532$ nm), and a diode laser ($\lambda = 785$ nm). The backscattered signal was collected through a $100\times$ objective and dispersed by a 1800 g/mm grating under triple subtractive mode. The spectra resolution is 1 cm^{-1} and the lowest resolvable frequency is 5 cm^{-1} . The size of the laser spot at the sample surface is approximately $1\text{ }\mu\text{m}$. Bi_2S_3 nanowires, nanosheets, and bulk powder were all examined by Raman scattering and showed similar spectra. We found that the signal-to-noise ratio was the best in nanosheets due to the much larger excited volume. However, we did not observe significant variation of the Raman features among all three types of samples. We therefore conclude that phonon confinement is negligible in these sample sizes.^{32,33} This is understandable because previous reports about silicon and gallium phosphide nanowires show that the phonon confinement effect becomes prominent only when the size is down to 10 nm, which is much smaller than the size of our nanostructures.^{34–36}

C. First-principles calculations

We employ density-functional theory (DFT) as implemented in the QUANTUM ESPRESSO³⁷ suite for our theoretical study. Bi_2S_3 belongs to the orthorhombic space group $Pbnm$ with 20 atoms per primitive cell, five of which are inequivalent. The unit cell is shown in Fig. 4.³⁸ A plane-wave basis set with a high-energy cutoff of 55 Ry is used to obtain reliable lattice constants and atomic positions. We use the local density approximation with pseudopotentials for S and

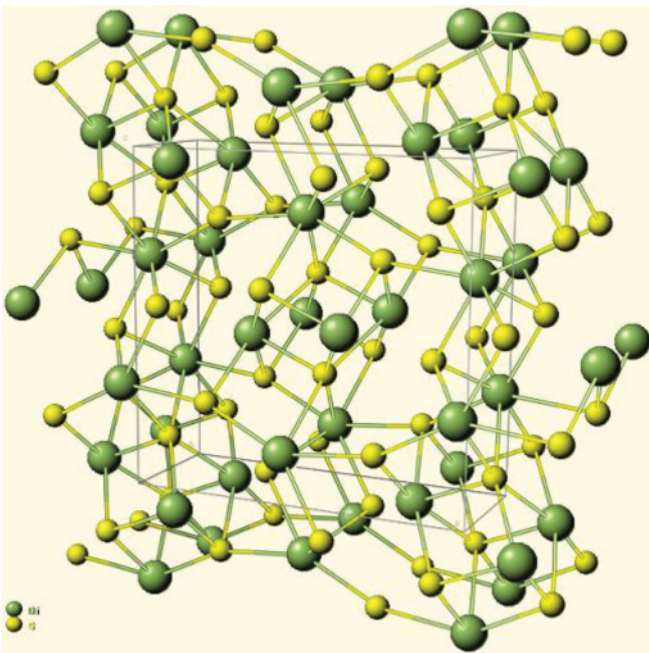


FIG. 4. (Color online) Primitive unit cell of orthorhombic Bi_2S_3 with 20 atoms, among which five are inequivalent.

TABLE I. Equilibrium lattice parameters a , b , and c for orthorhombic Bi_2S_3 from our first-principles calculations and experiment⁴⁰ showing a very good agreement.

	a (Å)	b (Å)	c (Å)	b/a	c/a
This work	10.950	11.103	3.974	1.014	0.363
Experiment ⁴⁰	11.137	11.297	3.981	1.014	0.357
Deviation (%)	-1.7	-1.7	-0.2	0.0	1.7

Bi generated according to the scheme proposed by Rappe *et al.*³⁹ A $3 \times 3 \times 9$ Monkhorst-Pack scheme is used for the k -point sampling. Convergence tests show that total energies are converged to 1 meV/atom .

1. Zone-center phonons

We first optimize the atomic coordinates and cell dimensions of Bi_2S_3 with residual forces of less than 10^{-3} eV/Å and stresses of less than $3 \times 10^{-5}\text{ eV/Å}^3$. Equilibrium lattice parameters obtained from the structural optimization are reported in Table I, which shows good agreement with experimental values of better than 2%.

The zone-center phonon frequencies are then calculated according to linear-response theory using density-functional perturbation theory (DFPT).^{41,42} For a 20-atom Bi_2S_3 primitive cell, there are 60 zone-center phonon modes that can be classified according to the D_{2h} point-group symmetry: $10A_g + 10B_{1g} + 5B_{2g} + 5B_{3g} + 5A_u + 5B_{1u} + 10B_{2u} + 10B_{3u}$. Of these, only A_g , B_{1g} , B_{2g} , and B_{3g} modes are Raman-active and hence may be compared with Raman experiments; the A_u mode is silent while the B_{1u} , B_{2u} , and B_{3u} modes are infrared-active. Thus, a total number of 27 Raman-active phonon modes are predicted, taking no account of the three zero-frequency acoustic phonon modes, which will be shown later in the phonon-dispersion curves.

2. Phonon dispersion

It is possible to further obtain the full phonon dispersion of Bi_2S_3 using DFPT. Such a calculation requires the evaluation of dynamical matrices $D(\mathbf{q})$ over a grid of \mathbf{q} points in the reciprocal space to construct the real-space interatomic force-constant matrix via Fourier interpolation. However, the DFPT calculation is to be performed at each \mathbf{q} and is hence computationally very demanding for the current system. As a result, we adopt a supercell force-constant approach^{43–46} for the phonon-dispersion curves. We note that this approach⁴³ is very similar to the interplanar force-constant approach^{47,48} in which entire planes of atoms are displaced to evaluate the interplanar force constants.

In the supercell force-constant approach, we displace each atom in the primitive cell from its equilibrium position in the a , b , and c directions by a distance of 0.015 Å . In order to reduce the effect of periodic images during each displacement, we use a $2 \times 2 \times 4$ orthorhombic supercell with 320 atoms and a $2 \times 2 \times 3$ Monkhorst-Pack mesh. We calculate the forces acting on all atoms in the supercell using the Hellman-Feynman theorem as implemented in QUANTUM ESPRESSO, allowing us to evaluate the interatomic force-constant matrix ϕ using a central finite-difference scheme. We have used a

cutoff radius of 15.0 Å centered on each atom when the force constants are evaluated. The resulting phonon frequencies at Γ and Z points (see Fig. 7) are essentially the same as those obtained from the density-functional perturbation theory.

Due to the polar character of Bi_2S_3 , the long-range Coulomb force gives rise to a macroscopic electric field, which can be observed in the nonvanishing Born effective charges \mathbf{Z}^* . This leads to the splitting of longitudinal-optical (LO) and transverse-optical (TO) phonons in Bi_2S_3 . However, the force-constant matrix ϕ calculated using the above-mentioned supercell method neglects these long-range interactions. In order to account for these interactions in the phonon dispersion, we employ a mixed-space approach proposed by Wang *et al.*⁴⁹ in which a correction factor is added to ϕ :

$$\Phi_{st}^{\alpha\beta} = \phi_{st}^{\alpha\beta} + \frac{\varphi_{st}^{\alpha\beta}}{N}, \quad (1)$$

where Φ is the corrected real-space interatomic force-constant matrix, ϕ is the short-range contribution as calculated previously using the supercell method, and φ is the correction factor due to long-range interactions. α and β run on the three spatial directions, while s and t run on all atoms in a primitive cell and on all primitive cells within the supercell. N is the number of primitive cells in the supercell.

We calculate the correction factor $\varphi_{st}^{\alpha\beta}$ using

$$\varphi_{st}^{\alpha\beta} = \frac{4\pi e^2}{\Omega} \frac{(\mathbf{q} \cdot \mathbf{Z}_s^*)_\alpha (\mathbf{q} \cdot \mathbf{Z}_t^*)_\beta}{\mathbf{q} \cdot \epsilon^\infty \cdot \mathbf{q}}, \quad (2)$$

where \mathbf{Z}^* is the Born effective charge tensor, ϵ^∞ is the high-frequency dielectric tensor, \mathbf{q} is the direction of approach to Γ , Ω is the volume of the primitive cell, and e is the magnitude of the electron charge. This requires the knowledge of both \mathbf{Z}^* and ϵ^∞ , which can easily be obtained from the DFPT calculation performed at Γ . The corrected force-constant matrix Φ is finally used to calculate the phonon-dispersion curves along lines of high symmetry in the Brillouin zone.

III. RESULTS AND DISCUSSION

A typical Raman spectrum from 30 to 300 cm^{-1} for Bi_2S_3 under 532 nm excitation is shown in Fig. 5. This was collected from a nanosheet on mica with a laser power of 3 mW, measured through a 10 \times objective. The Raman spectrum can be well fitted with 17 Lorentzian peaks. The reported Raman spectrum for powder-form bulk Bi_2S_3 shows four broad bands at 80, 185, 236, and 260 cm^{-1} , which are consistent with our spectrum shown in Fig. 5.²⁰ Koh *et al.* have also reported the 70, 96, 113, 125, 169, 186, 236, and 260 cm^{-1} bands in Bi_2S_3 thin films synthesized through single source precursor $\text{Bi}[\text{S}_2\text{CN}(\text{CH}_2)_4]_2\text{Cl} \cdot \text{CHCl}_3$.⁵⁰ Except for the peak at 113 cm^{-1} , all other peaks have been identified in our spectrum. More importantly, four strong low-frequency Raman peaks are observed for the first time at 33, 38, 46, and 53 cm^{-1} , all of which have full widths at half-maximum (FWHMs) of around 4 cm^{-1} . Such narrow FWHMs suggest long anharmonic lifetimes of the optical phonon vibrational modes.⁵¹

In order to further study phonons in Bi_2S_3 and assign the observed Raman peaks to specific phonon modes, we conducted first-principles calculations for the vibrational modes of

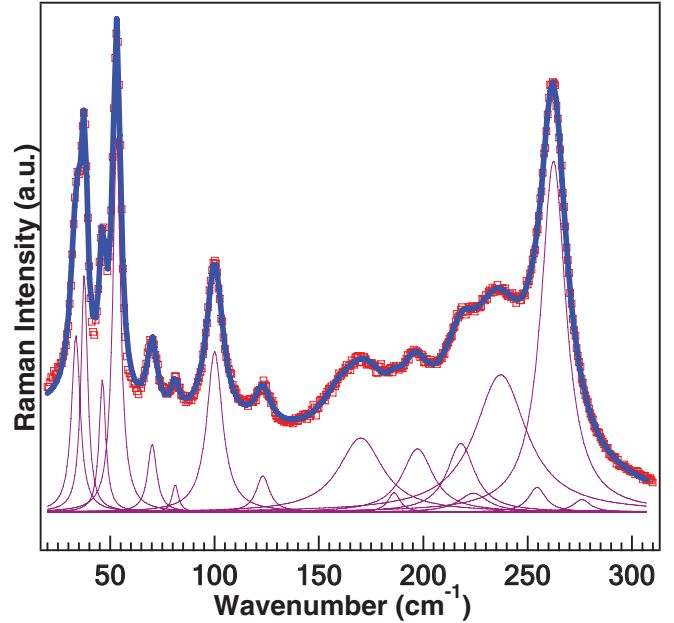


FIG. 5. (Color online) Raman spectrum of a Bi_2S_3 nanosheet under 532 nm excitation at 3 mW. The blue curve is a multi-Lorentzian fitting (with 17 peaks). The sharp peaks located at 33, 38, 46, and 53 cm^{-1} are observed for the first time.

orthorhombic Bi_2S_3 . Figure 6 shows schematically the normal modes of the four Raman modes of each symmetry (A_g , B_{1g} , B_{2g} , and B_{3g}) and one IR-active mode B_{3u} as obtained from the theoretical calculations. The phonon dispersion of Bi_2S_3 from the supercell method is shown in Fig. 7 together with the zone-center phonon frequencies calculated from DFPT. There is very good agreement at Γ between DFPT and the supercell method, with deviations of no more than 2.5% for the 60 Γ phonon modes. The long-range Coulomb interactions give rise to a dependence of zone-center phonons on the direction of approach to Γ . This is visible in the dispersion as differences in the zone-center frequencies between the $X \rightarrow \Gamma$ and $Y \rightarrow \Gamma$ directions. We note that the Raman modes that are being probed experimentally are transverse modes that are not

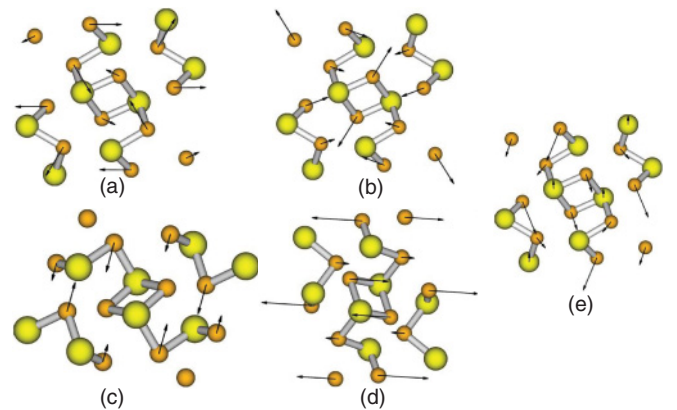


FIG. 6. (Color online) Representative vibrational normal modes of orthorhombic Bi_2S_3 from the first-principles calculations for the four Raman modes: (a) A_g , (b) B_{1g} , (c) B_{2g} , and (d) B_{3g} , as well as one infrared mode: (e) B_{3u} .

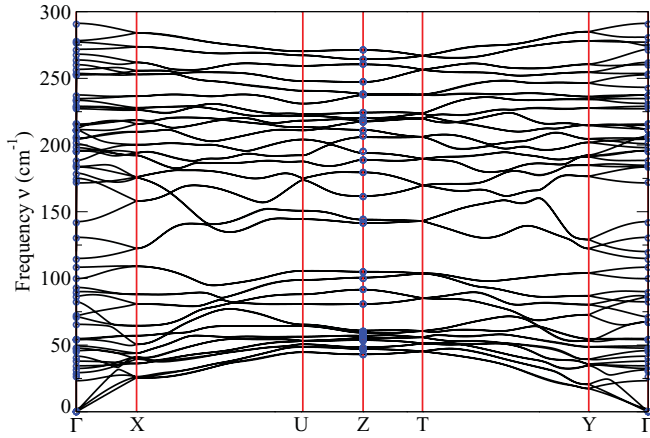


FIG. 7. (Color online) First-principles phonon-dispersion curves for orthorhombic Bi_2S_3 calculated using the supercell force-constant method. Blue circles are zone-center phonon frequencies calculated using density-functional perturbation theory. These zone-center phonon frequencies differ in the $X \rightarrow \Gamma$ and $Y \rightarrow \Gamma$ directions due to macroscopic electric fields in the polar compound. The selected k points are $\Gamma = (0,0,0)$, $X = (\frac{1}{2},0,0)$, $U = (\frac{1}{2},0,\frac{1}{2})$, $Z = (0,0,\frac{1}{2})$, $T = (0,\frac{1}{2},\frac{1}{2})$, and $Y = (0,\frac{1}{2},0)$.

influenced by the macroscopic electric field and hence do not suffer from LO-TO splitting.

Based on the first-principles calculations, we fitted our Raman spectrum with 17 Lorentzian peaks as shown by the blue curve in Fig. 5, which is in good agreement with the experimental data (red squares). The fitted peaks at 224, 254, and 276 cm^{-1} appear to be very weak but are confirmed by our wavelength- and power-dependent Raman scattering analysis, which will be discussed shortly. In addition, the

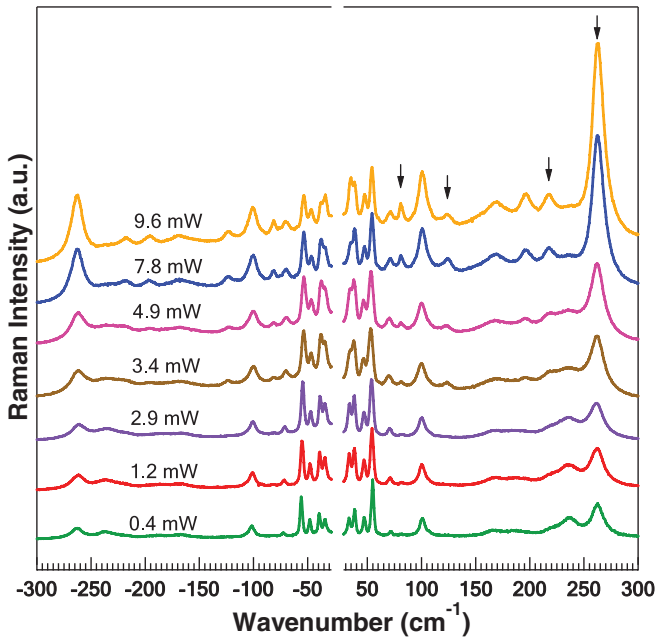


FIG. 8. (Color online) Power-dependent Raman spectra for a Bi_2S_3 nanosheet at the same position under 532 nm excitation. Raman bands at 81, 123, 237, and 262 cm^{-1} peaks (denoted by black arrows) show a pronounced dependence on excitation power.

TABLE II. Raman frequencies and corresponding phonon modes in Bi_2S_3 obtained through experiment and first-principles calculations. All the peaks match well except for the 123.1 cm^{-1} one, which we attribute to an IR-active B_{3u} mode.

Raman modes	Theoretical ν_p (cm^{-1})	Experimental ν_p (cm^{-1})	Infrared modes	Theoretical ν_p (cm^{-1})
B_{1g}	32.8	33.6		
B_{2g}	38.1	37.6		
A_g	40.4	46.3		
A_g	53.5	53.1		
A_g	70.9	70.1		
B_{1g}	86.0	81.1		
A_g	99.3	100.0		
		123.1	B_{3u}	119.3
B_{1g}	173.4	168.7		
A_g	184.0	186.0		
A_g	195.5	196.0		
A_g	211.1	218.7		
B_{3g}	228.2	224.1		
A_g	237.2	237.1		
A_g	253.3	254.5		
B_{1g}	260.7	262.4		
B_{1g}	277.3	276.3		

least-squares fit also improves significantly when these peaks are taken into account. According to the line-shape analysis, 17 Raman-active optical phonon peaks are observed. Taking into consideration the calculated Raman scattering cross sections, we assign these observed peaks to specific phonon modes. Table II summarizes both the measured experimental phonon frequencies and their corresponding theoretical phonon frequencies. The experimental results match well with our calculations, with the majority of differences being less than 2 cm^{-1} . Some phonons have a discrepancy of 5 cm^{-1} , which is still within the error limit. As shown in Table II, most observed phonons are A_g and B_{1g} modes. However, the peak at 123 cm^{-1} does not correspond to any predicted Raman mode, lying a large 15 cm^{-1} from the closest possible Raman modes. This distinct peak has a FWHM of around 7 cm^{-1} and has also been reported in Bi_2S_3 thin films.⁵⁰ Considering the calculated cross section, we propose that this 123 cm^{-1} peak does not correspond to a Raman-active mode but an IR-active B_{3u} phonon mode. This IR-active to Raman-active transition is generally due to the breaking of symmetry in bulk or nanostructures that can occur as a result of displacement defects in the lattice.⁵² This allows for the relaxation of Raman selection rules and enables IR-only modes to appear in the Raman spectrum. In addition to the peak frequencies, we also observe that the FWHMs for the phonon peaks vary from 4 to 30 cm^{-1} , indicating large differences in phonon lifetimes. The low-frequency peaks (less than 100 cm^{-1}) have much narrower FWHMs, and thus have much longer lifetimes than the high-frequency ones.

Having analyzed the overall Raman spectrum, we next examine the Raman scattering spectroscopy of individual Bi_2S_3 nanosheets as a function of the excitation power at room temperature. Bi_2S_3 is known for its low thermal conductivity,⁵³

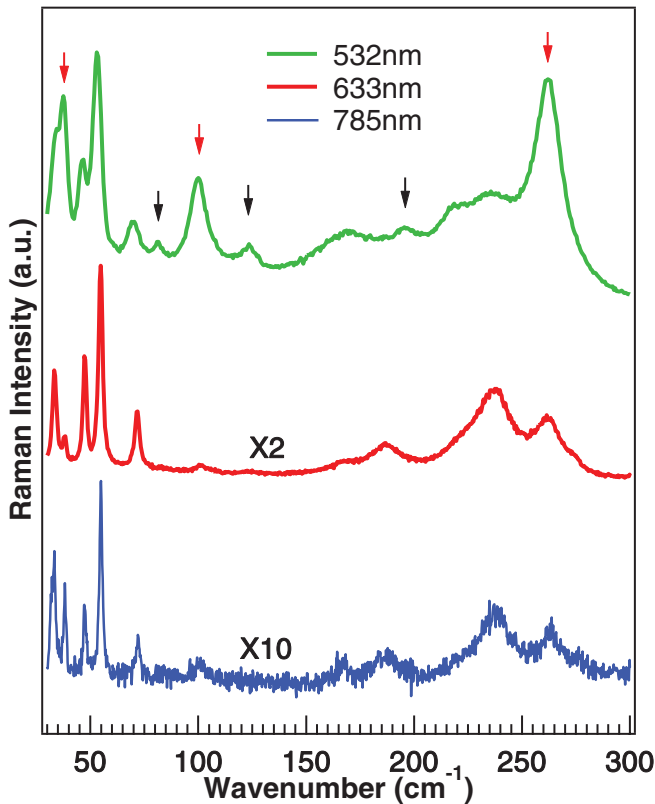


FIG. 9. (Color online) Raman spectra for a Bi_2S_3 nanosheet excited with three different lasers all at 3 mW. The relative intensities of the 38, 100, and 262 cm^{-1} Raman peaks (denoted by red arrows) with respect to that of the 53 cm^{-1} peak change considerably as the excitation wavelength changes. Raman modes at 81, 123, and 196 cm^{-1} (denoted by black arrows) appear only under the 532 nm excitation.

which can probably result in the sensitivity of its Raman spectrum to different excitation powers due to the laser heating effect. We conduct the power-dependent Raman scattering under 532 nm excitation on the same spot of a Bi_2S_3 nanosheet. Typical Stokes and anti-Stokes Raman spectra are shown in Fig. 8. The laser power is varied from 0.4 to 9.6 mW while keeping the integration time constant at 200 s. All spectra are normalized using the peak intensity of 53 cm^{-1} . We observed an interesting phenomenon, namely that particular phonon peaks (denoted by arrows in Fig. 8) are very sensitive to excitation power. The 81 and 123 cm^{-1} peaks can barely be observed below 3 mW excitation but become more pronounced as the power is increased. With a power of 7.8 mW, the 81 cm^{-1} peak becomes even stronger than the 70 cm^{-1} peak. The 262 cm^{-1} peak also shows a similar evolution. Using a power of less than 3 mW, the 196, 224, and 237 cm^{-1} peaks are indistinguishable and the Raman features appear more like humps instead of peaks. As the excitation power is increased, these peaks gradually separate and the intensities of the 196 and 224 cm^{-1} peaks become stronger. The improvement in Raman features under higher excitation power can be explained as the effect of laser annealing, which results in an improvement of crystalline quality at high laser power. However, the laser-induced heating does not seem sufficient to cause evident lattice expansion, as no peak shift is observed

among Raman spectra under different excitation powers. A notable exception to this rule is the 237 cm^{-1} peak, which weakens and finally disappears as the excitation power is increased. The reason behind this abnormal phenomenon is still unclear.

To further elucidate how Raman scattering depends on the excitation wavelength, we conducted experiments on the same Bi_2S_3 nanosheet using three different excitation lasers: 532, 632.8, and 785 nm. The laser power and integration time were kept at 3 mW and 200 s, respectively, for all three lasers. Figure 9 shows the Raman spectra under different excitation wavelengths. The Raman intensity is strongest under the 532 nm excitation and much weaker under the 785 nm excitation for the same integration time, in agreement with the well-known $1/\lambda^4$ (λ is the excitation wavelength) dependence of Raman scattering efficiencies.^{54,55} To facilitate a direct comparison among these three spectra, the 785 and 632.8 nm spectra have been multiplied by a factor of 10 and 2, respectively. Hence, the three spectra are normalized by the 53 cm^{-1} peak. Some phonon peaks are only identified in the 532 nm spectrum, such as those located at 81, 123, and 196 cm^{-1} (denoted by black arrows). The 276 cm^{-1} peak can be distinctly observed in the 632.8 and 785 nm spectra, but is very weak in the 532 nm spectrum, probably due to shadowing by the strong 262 cm^{-1} peak. We also note that some phonon peaks are remarkably sensitive to the excitation wavelengths as their relative intensities change significantly with respect to that of the 53 cm^{-1} peak. For example, the peaks located at 38, 100, and 262 cm^{-1} (denoted by red arrows) are especially pronounced under the 532 nm excitation. Generally, we find that some phonon modes in orthorhombic Bi_2S_3 show a strong dependence on the excitation wavelength, and certain modes exhibit a notable preference to the 532 nm excitation. This suggests that the scattering cross sections depend very much on the excitation wavelength.⁵⁶ This dependence usually happens in resonant Raman scattering, where Raman scattering efficiencies are expected to resonate when the laser frequencies approach the electronic band edge.⁵⁷ However, this explanation cannot be applied here because 532 nm is far from the band edge (located around 950 nm) of orthorhombic Bi_2S_3 . Further research is needed to fully understand the origin of the dependence.

IV. CONCLUSION

In conclusion, high-crystalline-quality Bi_2S_3 nanostructures have been synthesized through a simple physical vapor transport method. Mica substrates were used to obtain large-scale oriented nanosheets. A comprehensive Raman study was conducted experimentally and theoretically in order to investigate the lattice dynamics of orthorhombic Bi_2S_3 . First-principles calculations for bulk predict 27 Raman-active optical phonon modes of frequencies 30– 300 cm^{-1} , 16 of which agree well with our experimental measurements on nanostructures. The Raman peaks are successfully assigned to specific Raman symmetry modes except for the 123 cm^{-1} phonon mode, which we tentatively attribute to an IR B_{3u} mode that has probably become Raman-active as a result of

symmetry breaking caused by lattice displacement defects. Phonon-dispersion curves of Bi₂S₃ are also calculated using density-functional theory, with the effects of long-range interactions included. The variation of the Raman spectra under excitation lasers of different wavelengths illustrates the wavelength dependence of the scattering cross section for certain Raman modes.

ACKNOWLEDGMENTS

Q.X. thanks Dr. Shijie Wang and Ms. Lai Mun Wang for the help on TEM. Q.X. acknowledges the strong support from the Singapore National Research Foundation through a Singapore 2009 NRF fellowship grant (NRF-RF2009-06), a start-up grant (M58110061), and a New Initiative Fund (M58110100) from Nanyang Technological University.

*Qihua@ntu.edu.sg

- ¹S. H. Pawar, P. N. Bhosale, M. D. Uplane, and S. Tamhankar, *Thin Solid Films* **110**, 165 (1983).
- ²X. Peng, G. Meng, J. Zhang, L. Zhao, X. Wang, Y. Wang, and L. Zhang, *J. Phys. D* **34**, 3224 (2001).
- ³G. Konstantatos, L. Levina, J. Tang, and E. Sargent, *Nano Lett.* **8**, 4002 (2008).
- ⁴P. Boudjouk, M. P. Remington, D. G. Grier, B. R. Jarabek, and G. J. McCarthy, *Inorg. Chem.* **37**, 3538 (1998).
- ⁵J. Jie, W. Zhang, I. Bello, C.-S. Lee, and S.-T. Lee, *Nano Today* **5**, 313 (2010).
- ⁶O. Rabin, J. Manuel Perez, J. Grimm, G. Wojtkiewicz, and R. Weissleder, *Nat. Mater.* **5**, 118 (2006).
- ⁷K. Yao, Z. Zhang, X. Liang, Q. Chen, L. Peng, and Y. Yu, *J. Phys. Chem. B* **110**, 21408 (2006).
- ⁸L. Cademartiri, F. Scotognella, P. G. O'Brien, B. V. Lotsch, J. Thomson, S. Petrov, N. P. Kherani, and G. A. Ozin, *Nano Lett.* **9**, 1482 (2009).
- ⁹M. A. Pimenta, G. Dresselhaus, M. S. Dresselhaus, L. G. Cancado, A. Jorio, and R. Saito, *Phys. Chem. Chem. Phys.* **9**, 1276 (2007).
- ¹⁰Q. Xiong, J. Wang, O. Reese, L. C. Lew Yan Voon, and P. C. Eklund, *Nano Lett.* **4**, 1991 (2004).
- ¹¹Q. Xiong, R. Gupta, J. Wang, G. D. Mahan, L. C. Lew Yan Voon, and P. C. Eklund, *Solid State Phenom.* **121-123**, 955 (2007).
- ¹²R. Gupta, Q. Xiong, G. D. Mahan, and P. C. Eklund, *Nano Lett.* **3**, 1745 (2003).
- ¹³Q. Xiong, G. Chen, H. R. Gutierrez, and P. C. Eklund, *Appl. Phys. A* **85**, 299 (2006).
- ¹⁴M. S. Dresselhaus, A. Jorio, M. Hofmann, G. Dresselhaus, and R. Saito, *Nano Lett.* **10**, 751 (2010).
- ¹⁵J. Zhang, Z. Peng, A. Soni, Y. Zhao, Y. Xiong, B. Peng, J. Wang, M. S. Dresselhaus, and Q. Xiong, *Nano Lett.* **11**, 2407 (2011).
- ¹⁶X. Shen, G. Yin, W. Zhang, and Z. Xu, *Solid State Commun.* **140**, 116 (2006).
- ¹⁷C. Pilapong, T. Thongtem, and S. Thongtem, *J. Phys. Chem. Solids* **71**, 712 (2010).
- ¹⁸Q. Han, Y. Sun, X. Wang, L. Chen, X. Yang, and L. Lu, *J. Alloys Compd.* **481**, 520 (2009).
- ¹⁹J. Ota and S. K. Srivastava, *J. Phys. Chem. C* **111**, 12260 (2007).
- ²⁰K. Trentelman, *J. Raman Spectrosc.* **40**, 585 (2009).
- ²¹Y. Yu and W. Sun, *Mater. Lett.* **63**, 1917 (2009).
- ²²H. Bao *et al.*, *Nanotechnology*. **19**, 335302 (2008).
- ²³K. Yao, W. Gong, Y. Hu, X. Liang, Q. Chen, and L. Peng, *J. Phys. Chem. C* **112**, 8721 (2008).
- ²⁴X. Yang, X. Wang, and Z. Zhang, *Mater. Chem. Phys.* **95**, 154 (2006).
- ²⁵D. Wang, C. Hao, W. Zheng, X. Ma, D. Chu, Q. Peng, and Y. Li, *Nano Res.* **2**, 130 (2009).
- ²⁶Y. Sun, Q. Han, J. Lu, X. Yang, L. Lu, and X. Wang, *Mater. Lett.* **62**, 3730 (2008).
- ²⁷S. H. Yu, J. Yang, Y. S. Wu, Z. H. Han, Y. Xie, and Y. Qian, *Mater. Res. Bull.* **33**, 1661 (1998).
- ²⁸O. C. Monteiro, T. Trindade, J. H. Park, and P. O'Brien, *Chem. Vapor. Depos.* **6**, 230 (2000).
- ²⁹V. V. Killedar, S. N. Katore, and C. H. Bhosale, *Mater. Chem. Phys.* **64**, 166 (2000).
- ³⁰J. Xu, N. Petkov, X. Wu, D. Iacopino, A. J. Quinn, G. Redmond, T. Bein, M. A. Morris, and J. D. Holmes, *Chem. Phys. Chem.* **8**, 235 (2007).
- ³¹M. I. B. Utama, Z. Peng, R. Chen, B. Peng, X. Xu, Y. Dong, L. M. Wong, S. Wang, H. Sun, and Q. Xiong, *Nano Lett.* **11**, 3051 (2011).
- ³²H. Richter, Z. P. Wang, and L. Ley, *Solid State Commun.* **39**, 625 (1981).
- ³³I. H. Campbell and P. M. Fauchet, *Solid State Commun.* **58**, 739 (1986).
- ³⁴S. Piscanec, M. Cantoro, A. C. Ferrari, J. A. Zapien, Y. Lifshitz, S. T. Lee, S. Hofmann, and J. Robertson, *Phys. Rev. B* **68**, 241312 (2003).
- ³⁵K. W. Adu, H. R. Gutierrez, U. J. Kim, and P. C. Eklund, *Phys. Rev. B* **73**, 155333 (2006).
- ³⁶Q. Xiong, R. Gupta, K. W. Adu, E. C. Dickey, G. D. Lian, D. Tham, J. E. Fischer, and P. C. Eklund, *J. Nanosci. Nanotechnol.* **3**, 1533 (2003).
- ³⁷P. Giannozzi *et al.*, *J. Phys. Condens. Matter* **21**, 395502 (2009).
- ³⁸Mineralogy Database [<http://webmineral.com>].
- ³⁹A. M. Rappe, K. M. Rabe, E. Kaxiras, and J. D. Joannopoulos, *Phys. Rev. B* **41**, 1227 (1990).
- ⁴⁰K. Łukaszewicz, J. Stępień-Damm, A. Pietraszko, A. Kajokas, and J. Grigas, *Pol. J. Chem.* **73**, 541 (1999).
- ⁴¹S. Baroni, P. Giannozzi, and A. Testa, *Phys. Rev. Lett.* **58**, 1861 (1987).
- ⁴²S. Baroni, S. de Gironcoli, A. Dal Corso, and P. Giannozzi, *Rev. Mod. Phys.* **73**, 515 (2001).
- ⁴³G. Kresse, J. Furthmuller, and J. Hafner, *Europhys. Lett.* **32**, 729 (1995).
- ⁴⁴C. K. Gan, Y. P. Feng, and D. J. Srolovitz, *Phys. Rev. B* **73**, 235214 (2006).
- ⁴⁵C. K. Gan, X. F. Fan, and J. L. Kuo, *Comput. Mater. Sci.* **49**, S29 (2010).
- ⁴⁶Z. W. Tan, J.-S. Wang, and C. K. Gan, *Nano Lett.* **11**, 214 (2011).
- ⁴⁷K. Kunc and R. M. Martin, *Phys. Rev. Lett.* **48**, 406 (1982).
- ⁴⁸K. Kunc and P. G. Dacosta, *Phys. Rev. B* **32**, 2010 (1985).

- ⁴⁹Y. Wang, J. J. Wang, W. Y. Wang, Z. G. Mei, S. L. Shang, L. Q. Chen, and Z. K. Liu, *J. Phys. Condens. Matter* **22**, 202201 (2010).
- ⁵⁰Y. W. Koh, C. S. Lai, A. Y. Du, E. R. T. Tiekink, and K. P. Loh, *Chem. Mater.* **15**, 4544 (2003).
- ⁵¹A. Debernardi, *Phys. Rev. B* **57**, 12847 (1998).
- ⁵²D. J. Arenas, L. V. Gasparov, W. Qiu, J. C. Nino, C. H. Patterson, and D. B. Tanner, *Phys. Rev. B* **82**, 214302 (2010).
- ⁵³B. Chen, C. Uher, L. Iordanidis, and M. G. Kanatzidis, *Chem. Mater.* **9**, 1655 (1997).
- ⁵⁴D. A. Long, McGraw-Hill, *Raman Spectroscopy* (McGraw-Hill, New York, 1977).
- ⁵⁵D. P. Strommen and K. Nakamoto, *Laboratory Raman Spectroscopy* (Wiley, New York, 1984).
- ⁵⁶W. H. Weber and R. Merlin, *Raman Scattering in Materials Science* (Springer, New York, 2000).
- ⁵⁷J. M. Calleja and M. Cardona, *Phys. Rev. B* **16**, 3753 (1977).